Pure and Applied Geophysics

Ground Deformation and Source Fault Model of the Mw 5.7 Xegar (Tibetan Plateau) 2020 Earthquake, Based on InSAR Observation

Chengtao Li,[1,2,3] Qi Li,[1,2,3] Kai Tan,[1,2,3] Yong Huang,[1,4] and Xiaofei Lu[1,2,3]

Abstract—An Mw 5.7 earthquake occurred in Xegar, Tingri Basin, Tibetan Plateau, on 20 March 2020. Determining the precise focal mechanism solution is helpful for understanding the seismogenic mechanism and the geodynamic process of this earthquake. Here, we used Sentinel-1A data to obtain line-of-sight coseismic deformation. Fault geometric parameters and coseismic slip distribution can be estimated with the Bayesian method and the steepest descent method, respectively. The inversions show that the strike of the seismogenic fault is ∼ 330.0°, with a dip angle of ∼ 62.7°. The main rupture zone covers an area of ∼ 5 × 5 km². Only one slip asperity appears at a depth of 1.9–5.0 km, the maximum slip on the fault is 0.98 m at a depth of 3.26 km, with a centroid location of 87.40° E, 28.66° N, and the mean rake angle is ∼ −104.6°. The results reveal that this earthquake is dominated by normal faulting, and the derived seismic moment is ∼ 3.23 × 10¹⁷ Nm (Mw 5.6). Furthermore, it is found that the 2015 Mw 7.9 Gorkha earthquake played a key role in triggering the 2020 Mw 5.7 Xegar earthquake based on calculation of the coseismic and postseismic Coulomb failure stress with different viscosities and depths.

Keywords: Xegar earthquake, coseismic deformation, coseismic slip distribution, coulomb failure stress.

1. Introduction

According to the Global Centroid Moment Tensor (GCMT, https://www.globalcmt.org/CMTsearch.html), a 12-km-deep Mw 5.7 earthquake stuck Xegar town in the Tingri Basin of the southern Tibetan Plateau on 20 March 2020, the epicenter of which was located at 87.42° E and 28.51° N. The focal mechanism solution determined by the United States Geological Survey (USGS, https://earthquake.usgs.gov/earthquakes/search/) indicates that the earthquake is a normal faulting event. Since the Miocene, the Tibetan Plateau has experienced a wide range of extension, which not only regulates the deformation of the convergence of India and Eurasia but is also closely related to the uplift of the plateau (Molnar & Tapponnier, 1978; Zhang et al., 2002). The thrust faults are mainly developed near the Himalayan main boundary faults (MBT), while the south Tibet region to the north has east–west stretching tectonics resulting from the near south–north squeezing tectonics (Yong, 2012). Many normal faults have been developed: these include the South Tibetan Detachment System (STDS), the Xainza–Dinggye fault (XDF), and the Yadong–Gulu fault (YGF). In recent years, seismic events of Mw ≥ 5.0 are relatively common in south Tibet (Fig. 1). These are mostly characterized by normal faulting, indicating that the region is mainly affected by tensile stress. As early as 25 April 2015, an earthquake of Ms 5.9 occurred not far from the southern side of this earthquake, which was also a normal fault tensional activity event, categorized as a normal fault-type earthquake of the STDS (Dan et al., 2016). Zha and Dai (2017) suggest that the 2015 Gorkha earthquake triggered the 2015 Ms 5.9 earthquake. Through detailed study of this Mw 5.7 earthquake, we can understand the seismogenic characteristics of the Tingri Basin and attempt to discuss the influence of the 2015 Gorkha earthquake on the 2020 Xegar earthquake.

[1] Institute of Seismology, China Earthquake Administration, Wuhan 430071, China. E-mail: lict@cgps.ac.cn; today1352600@163.com; whgpstan@163.com; 568419166@qq.com; luxiaofei@cgps.ac.cn

[2] Key Laboratory of Earthquake Geodesy, CEA, Wuhan 430071, China.

[3] Hubei Earthquake Administration, Wuhan 430071, China.

[4] State Key Laboratory of Geodesy and Earth's Dynamics, Innovation Academy for Precision Measurement Science and Technology, Chinese Academy of Sciences, Wuhan 430077, China.
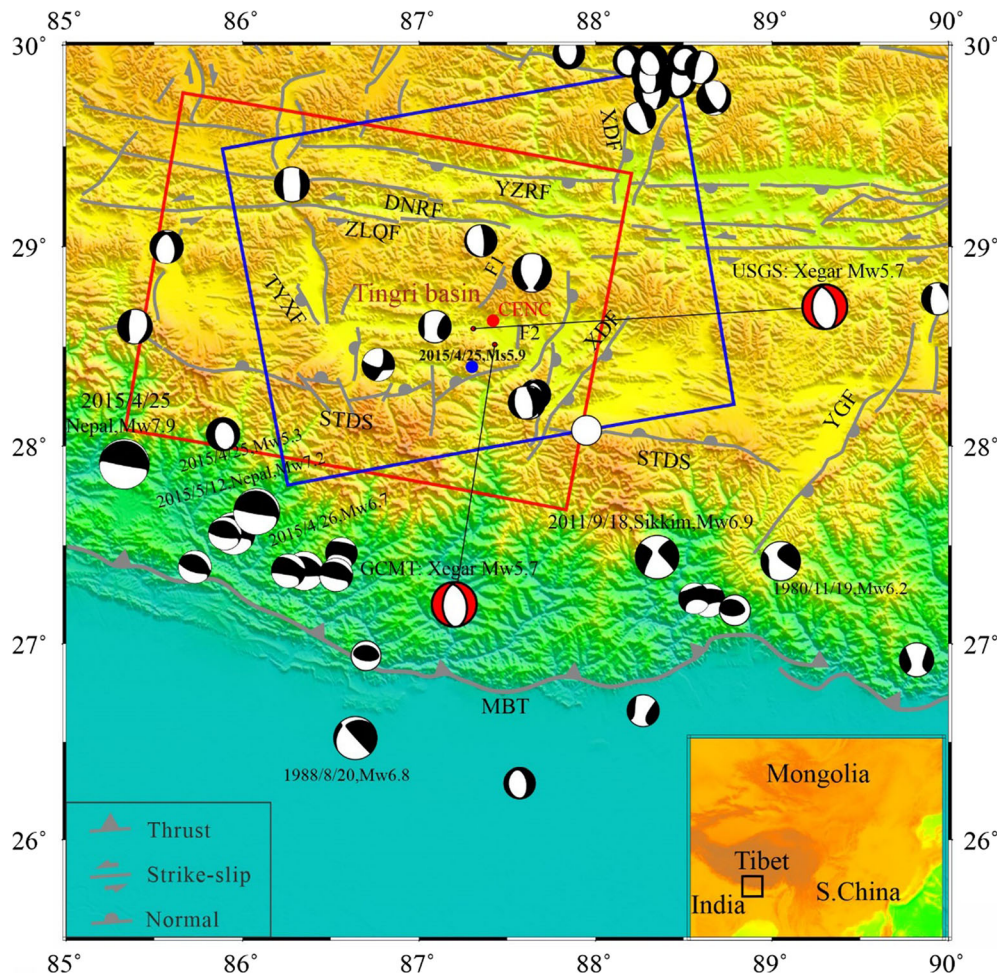
Figure 1
Tectonic and seismic background map. The red rectangle represents the range of descending track 121, the blue rectangle represents the range of ascending track 12. Red dot: the epicenter of the earthquake measured by the China Earthquake Networks Center (CENC) on 20 March 2020; USGS: focal mechanism solution of this earthquake given by United States Geological Survey; GCMT: the focal mechanism solution given by Columbia University; Blue dot: epicenter of the Ms 5.9 earthquake on 25 April 2015; Other focal mechanism solutions: earthquakes of Mw ≥ 5 from 1976 to 2020 (GCMT). *STDS* South Tibetan Detachment system, *XDF* Xainza-Dinggye fault, *YGF* Yadong-Gulu fault, *YZRF* Yarlung Zangbo River fault, *TYXF* Tangra Yumco-Xuru co-fault, *MBT* main boundary thrust fault of Himalaya, *ZLQF* Zanda-Lhazê-Qiongduojiang fault, *DNRF* Darjeeling-Ngamring-Rinbung fault, F1 and F2 are anonymous faults

Recently, Global Positioning System (GPS), seismic wave, and interferometric synthetic aperture radar (InSAR) technologies have made considerable contributions to seismological research (Fadil et al., 2021; Li et al., 2018; Melgar et al., 2015; Wang et al., 2011, 2020; Wen et al., 2016; Zhao et al., 2019). However, there are few GPS stations near the 2020 Xegar earthquake, and no obvious coseismic deformations have been observed. In addition, although seismic waves are often used to determine the

centroid and focal mechanism solution, sometimes, under the influence of station distribution, the strike and dip angle of the seismogenic fault and the centroid location obtained by inversion are not accurate (Ghayournajarkar & Fukushima, 2022; Weston et al., 2011, 2012). The centroid locations provided by USGS, CENC (China Earthquake Networks Center, http://news.ceic.ac.cn/) and GCMT are also different, complicating subsequent studies on coseismic rupture. Fortunately, near-field geodetic data, such as

InSAR data, can well constrain the geometric parameters (location and rupture geometry). At the same time, InSAR data have advantages of high spatial positioning, high deformation sensitivity, high spatial resolution. Therefore, the differential InSAR (DInSAR) technique is widely used in researching crustal deformation. Moreover, determining the exact locations of centroid and seismogenic fault parameters and studying the coseismic slip distribution of small and moderate earthquakes are important research areas (Zhu et al., 2021).

In this study, the coseismic deformation caused by the 2020 Mw 5.7 Xegar earthquake was measured using the DInSAR technique with ascending and descending Sentinel-1A data, and the Bayesian method was adopted to study the fault geometric parameters (Vasyura-Bathke et al., 2020). Then, the coseismic slip distribution can be inverted with the steepest descent method (SDM) (Wang et al., 2013). Additionally, we analyze the dip orientation of the seismogenic fault comprehensively from the residual map, 2.5D deformation field and the aftershock distribution. Finally, we estimate the impact of the 2015 Mw 7.9 Gorkha earthquake on the 2020 Mw 5.7 Xegar earthquake by calculating the coseismic and postseismic Coulomb failure stress changes (ΔCFS). These results provide a reference value for understanding the deformation characteristics and seismogenic structure of the Xegar earthquake.

2. InSAR Data

Sentinel-1A Interferometric Wide Swath data are used in this study. We downloaded the following Sentinel-1A data from the European Space Agency (ESA) (https://sentinel.esa.int/): For the ascending track 12, the pre-earthquake acquisition is on 8 March 2020, and the repeat pass is on 20 March 2020. For the descending track 121, the pre-earthquake and the post-earthquake acquisitions are on 16 March 2020 and on 28 March 2020, respectively. The detailed information is shown in Table 1.

Interferometric processing was performed with ISCE (InSAR Scientific Computing Environment) open-source software (Rosen et al., 2012). The DInSAR method was utilized to produce coseismic deformation interferograms (Fig. 2) (Massonnet et al., 1993). To suppress the noise, the multi-look factor in the range and azimuth was set as 5:1. The precision orbit data were the satellite precision orbit determination (POD) (precise orbit ephemerides) provided by the ESA (https://scihub.copernicus.eu/gnss/#/home). The Shuttle Radar Topography Mission (SRTM) digital elevation model with a resolution of 30 m was adopted to eliminate the influence of the topographic phase (Farr et al., 2007). The signal-to-noise ratio (SNR) was increased by Goldstein filtering (Goldstein & Werner, 1998). Then, the interferograms were unwrapped with the statistical-cost, network-flow algorithm for phase-unwrapping (SNAPHU) (Chen & Zebker, 2002). In order to reduce the effects of phase noise, we mask out water bodies and areas with spatial coherence less than 0.4. Finally, the unwrapped interferograms were geocoded to the World Geodetic System 1984 (WGS84).

Combining the coseismic interferograms and LOS deformation field shows that the surface deformation of the Mw 5.7 earthquake has a small range of influence, being $\sim 5 \times 5$ km (Figs. 2 and 4). For the ascending and descending tracks, the main deformation area is dominated by subsidence. The maximum

Table 1

Detailed parameters of sentinel-1A

Master	Slave	Δt/days	$B_\perp$/m	Incident angle (°)	Azimuth angle (°)	Orbit	Polarization
20200308	20200320	12	−20.02	39.67°	−10.56	Ascending	VV
20200316	20200328	12	26.62	36.02°	−169.51	Descending	VV

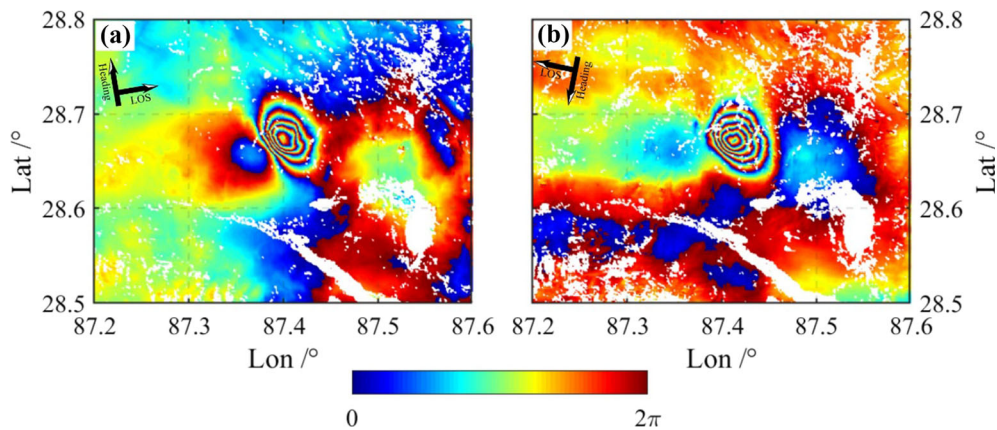Δt represents the temporal baseline. $B_\perp$ means the perpendicular baseline

Figure 2
Coseismic interferograms of the Xegar earthquake. **a** and **b** are coseismic interferograms for the ascending track and descending track, respectively

displacement values in the LOS direction are 12.6 and 15.7 cm, respectively.

3. Inversion of Fault Geometry and Coseismic Slip Distribution

We down-sampled the LOS deformation field using the quadtree method to accelerate the inversion process and suppress noise (Jónsson et al., 2002). Given the importance of the deformation of the near field, we set different thresholds in the down-sampling process. The near-field deformation was sampled densely, whereas the far-field region was sampled sparsely. In this way, the deformation characteristics of the near field were retained to the greatest extent, and the negative impact of the far-field error and noise on inversion was reduced to a certain extent. After quadtree down-sampling, 817 and 848 data points were reserved for the ascending and descending tracks, respectively (Fig. 4).

3.1. Inversion of Fault Geometric Parameters

In this paper, the fault plane is treated as a uniform plane to obtain fault parameters (such as length, width, dip, strike). The Bayesian Earthquake Analysis Tool (BEAT) was applied to determine the fault geometry parameters and their uncertainties (Vasyura-Bathke et al., 2020). Then, the sequential

Monte Carlo (SMC) algorithm was used to assess the posterior probability distribution (Moral et al., 2006).

The marginal posterior probability distribution of parameters exhibited discrete variability of the retrieved fault parameters (Fig. 3). The red lines in the histogram represent the maximum a posteriori (MAP) solution, which represents the optimal values. The lower limit of the confidence interval is taken as 2.5% after sorting, and the upper limit of the confidence interval is taken as 97.5% after sorting, so that the region between the two gives the 95% confidence interval of each parameter. The 2.5 and 97.5% limits of the posterior probability density functions of the fault parameters are reported. Finally, the inversion results of the fault geometric parameters are shown (Table 2). East_shift and North_shift represent offsets relative to the reference point (87.42° E, 28.51° N, the epicenter location provided by GCMT) in the UTM coordinate system, geometrically representing the central point of the upper boundary of the fault, transformed by coordinates to (longitude = 87.392° E, and latitude = 28.660° N). In addition, the strike, dip, and rake angle are 330.0° ± 1.35, 62.7° ± 0.96, and −109.2° ± 2.41, respectively

When inverting the fault geometric parameters, the residual results can be used to measure the quality of inversion (Fig. 4). The simulated values fit well with the observed coseismic LOS displacement in both the ascending and descending tracks. The root-
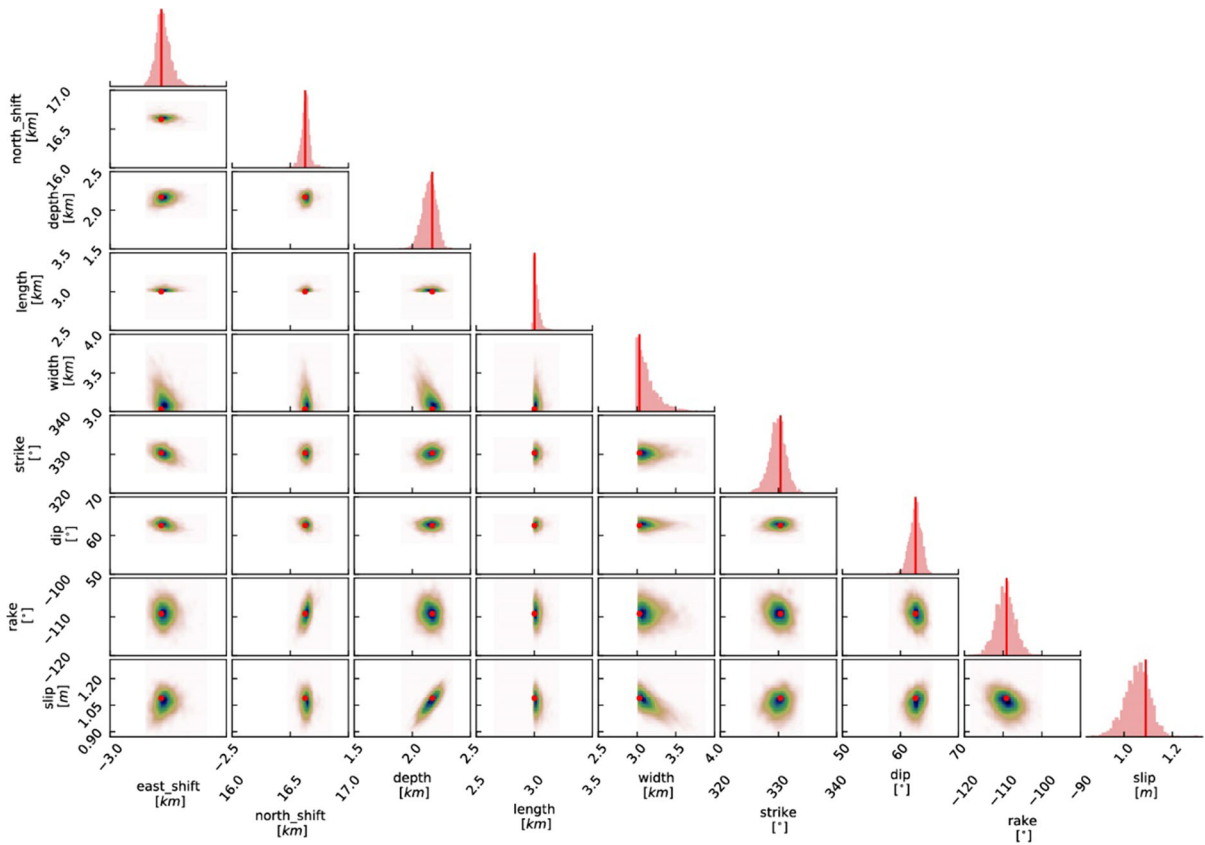
Figure 3

Marginal posterior probability distributions for the fault model parameters for the 2020 Mw 5.7 Xegar earthquake. Histograms show the posteriori probability distribution of fault parameters, red lines represent the maximum a posteriori (MAP) solution. Scatter plots are contoured according to frequency, which show trade-offs between parameters. Cold colors indicate low frequency, and warm colors indicate high frequency

Table 2

Inversion results of fault geometric parameters

Parameter	MAP	Std	2.5%	97.5%
Fault length (km)	3.03	0.03	3.00	3.13
Fault width (km)	3.14	0.13	3.00	3.61
North_shift (km)	16.635	0.03	16.530	16.753
East_shift (km)	−2.769	0.03	−2.847	−2.679
Strike (°)	330.00	1.35	325.95	333.05
Dip (°)	62.70	0.96	60.10	64.98
Rake (°)	−109.20	2.41	−115.10	−102.56
Depth (km)	2.15	0.06	2.00	2.29
Slip (m)	1.06	0.05	0.92	1.18

mean-square (RMS) misfit residuals are all 1.0 cm. Thus, we consider that the parameters of the inversion are reasonable.

3.2. Inversion of Coseismic Slip Distribution

After the fault geometric parameters were determined from the Bayesian method, the steepest descent method (SDM) was adopted to study the coseismic slip distribution (Wang et al., 2013). The stratification of the crust is extracted from the Crust 1.0 model (Laske et al., 2013). The surface
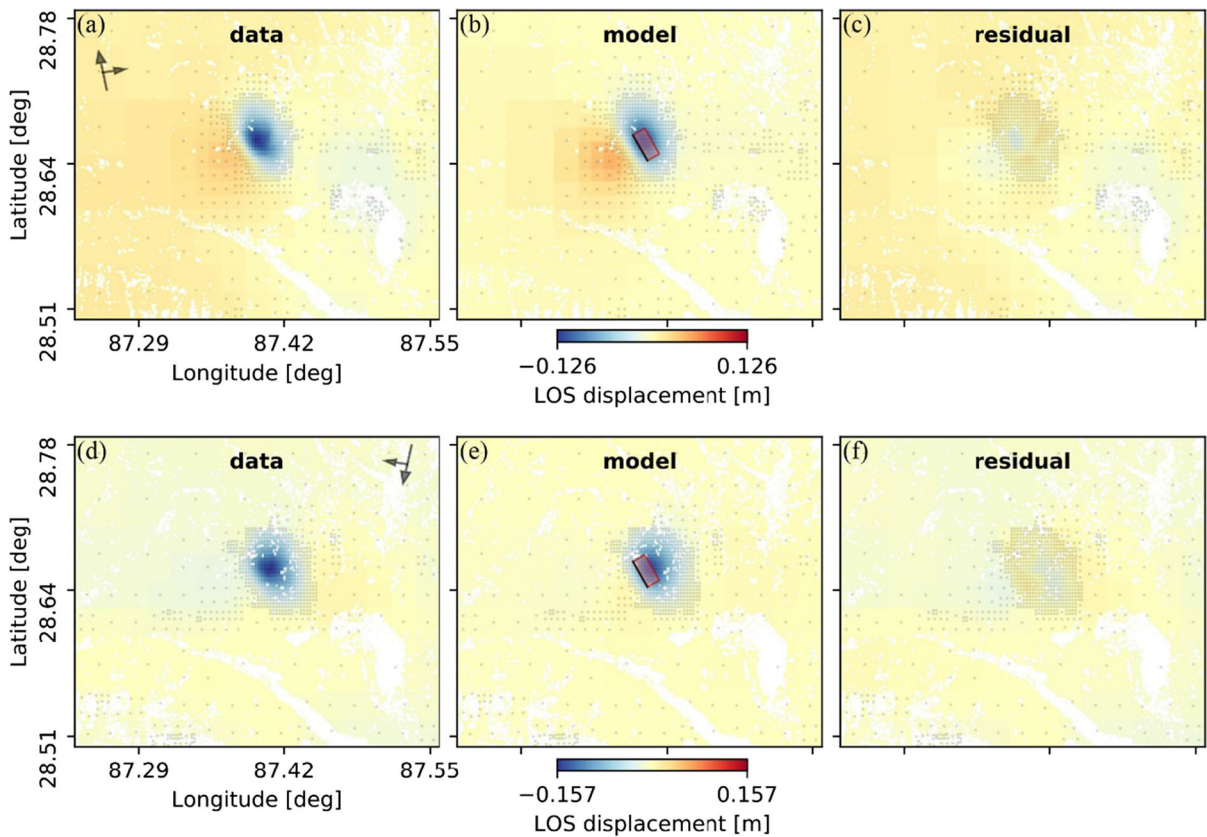
Figure 4
The uniform slip inversion result of the 2020 Xegar earthquake. **a** Observed, **b** modeled, and **c** residual values of the ascending track. **d** Observed, **e** modeled, and **f** residual values of the descending track. Gray points indicate down-sampling data

Table 3

Focal parameters for the 2020 Xegar earthquake comparison by various agencies

Sources	Strike (°)	Dip (°)	Rake (°)	Depth (km)	Mw	Centroid (°)	
						Lon	Lat
This study	330	62.7	−104.6	3.26	5.6	87.40	28.66
USGS	343	49	−101	10	5.7	87.308	28.590
GCMT	345	45	−103	12	5.7	87.42	28.51
CENC	–	–	–	10	Ms 5.9	87.42	28.63

Sources: USGS: https://earthquake.usgs.gov/earthquakes/eventpage/us70008cld/moment-tensor. GCMT: https://www.globalcmt.org/CMTsearch.html. CENC: http://news.ceic.ac.cn/

deformation caused by fault dislocation was calculated by using the Okada elastic dislocation theory (Okada, 1985). It fits the observed values and minimizes the roughness of the slip distribution as follows:

$$\|W(GS - d)\|^2 + \alpha^2 \|Ls\|^2 = min \qquad (1)$$

where W is the weight matrix of the observed value, and G is Green's function, which can be calculated through the elastic dislocation model based on the stratification of the crust in semi-infinite space (Wang
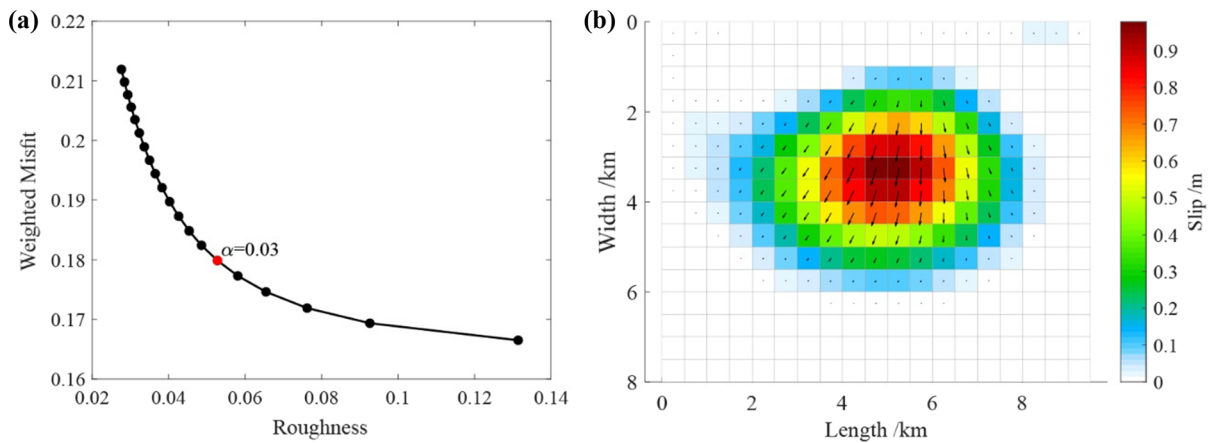
Figure 5

a Trade-off curve between model roughness and weighted misfit, **b** Coseismic slip distribution of northeast-dipping model inverted by InSAR

et al., 2003), d is the value of the LOS displacement, α is the smoothing factor, the trade-off curve between the model roughness and the data misfit calculated by different smoothing factors is usually used to select the optimal slip model. L represents the second-order finite difference approximation of the Laplacian operator. S is the strike and dip slip on each sub-fault.

The fault geometric parameters were set as follows: the strike was set at 330° and dip angle was set at 62.7° (Table 3), the fault plane was expanded to 9.5 km along the strike and 8 km along
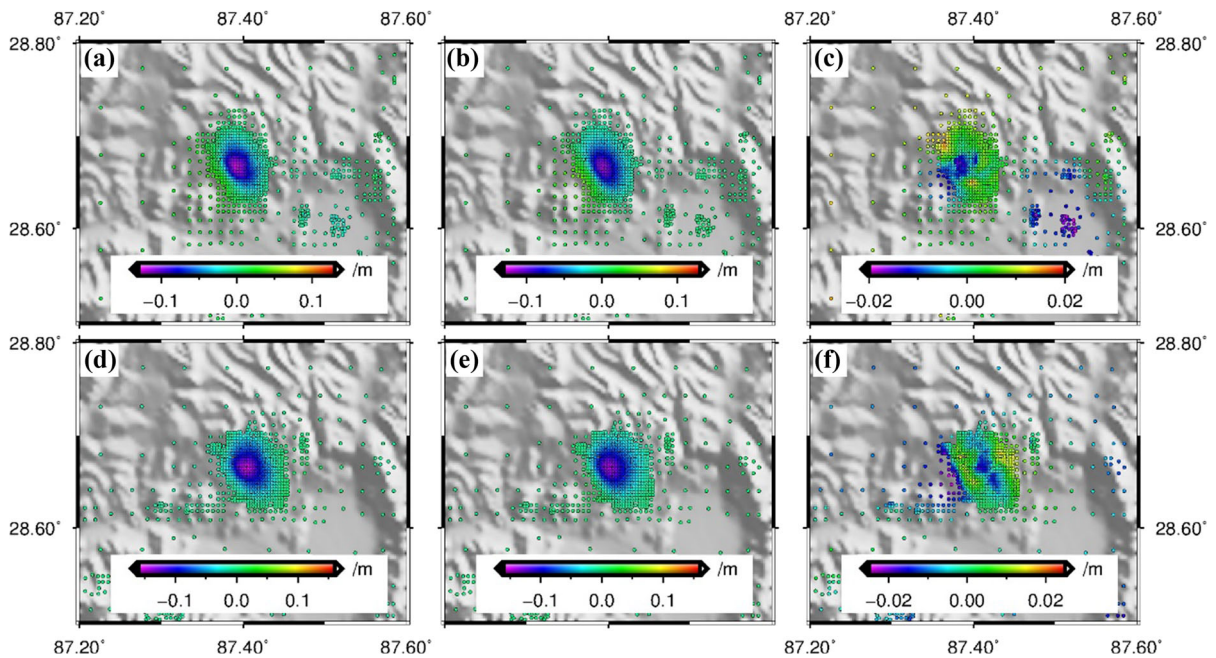

Figure 6

The distributed slip inversion result of the northeast-dipping model. **a** Observed, **b** modeled, and **c** residual values of the ascending track. **d** Observed, **e** modeled, and **f** residual values of the descending track

the down-dip direction, respectively. The origin of coordinates was taken as the central point of the top boundary of the fault (87.392° E, 28.660° N) and the corresponding depth was ∼ 2.15 km.

Figure 5a shows the trade-off curve between the model roughness and the weighted misfit. In this study, we chose the solution with the smoothing factor of 0.03 as the final inversion result. The coseismic slip distribution indicates that the main rupture zone covers an area of ∼ 5 × 5 km^2 (Fig. 5b), and only one slip asperity appears, at a depth of 1.9–5.0 km. The rake angle in the main rupture zone is nearly vertical, with an average rake angle of −104.6°. The coseismic rupture is mainly characterized by normal extension, with a small amount of right-lateral strike-slip. The maximum slip on the fault is ∼ 0.98 m, located at (87.40° E, 28.66° N) and buried at a depth of 3.26 km, which we call the centroid location. The seismic moment released by the earthquake is ∼ 3.23 × 10^{17} Nm, or equivalent to Mw 5.6, which is consistent with the result of Gao et al. (2021) but slightly smaller than the seismic moment of USGS and GCMT.

Figure 6 shows the modeled displacements and residuals for the northeast-dipping model. The ascending track residual ranges from −1.98 to 1.43 cm, with an RMS of 0.71 cm. In comparison, the residual of the descending track is slightly larger, with a residual range from −2.39 to 1.61 cm and an RMS of 0.77 cm. In general, we consider this inversion result as representing the best fit for the coseismic slip model.

4. Discussion

4.1. Comparison of the Location of Centroids

In seismogenic fault inversion and seismology research, the location of the centroid is indispensable, and its accuracy can often affect subsequent analysis and results. The locations of centroids provided by different agencies are often different. For comparison, we calculated the horizontal distance between seismically derived centroids and InSAR-derived centroid. The white star located at 87.40° E, 28.66° N represents the location of the geodetic centroid

location determined from InSAR data. Meanwhile, it is located near the center of the LOS deformation field, which is more consistent with the accurate location of the centroid. According to Table 3, the centroid location is closest to the point measured by CENC, with a spatial difference of 3.9 km. However, it is far from the centroids measured by USGS and GCMT, with differences of ∼ 11.9 and ∼ 16.7 km, respectively. This may be mainly affected by the distribution of the seismic network and the location of the seismoscopes. Moreover, these deviations may be caused by different speed models used by different agencies. The centroid measured by the near-field data is significantly more accurate than those from USGS and GCMT. In addition, some researchers studied 10 earthquakes in Iran and Japan and concluded that InSAR is a useful tool to accurately determine the fault parameters (location and rupture geometry) of shallow inland earthquakes (Ghayour-najarkar & Fukushima, 2022). Compared to teleseismic techniques, LOS displacement measurements from InSAR provide more accurate estimates of earthquake location (Weston et al., 2011, 2012; Zhu et al., 2021). Those indicate that the near-field InSAR deformation field data can be used to better determine the centroid location of moderate earthquakes.

4.2. The Impact of GACOS-Based Correction on the Model

Atmospheric effect is one of the main error sources of InSAR. We applied the atmospheric delay estimated by the Generic Atmospheric Correction Online Service for InSAR (GACOS), which utilizes the Iterative Tropospheric Decomposition (ITD) model (Yu et al., 2017, 2018). For most small-to-moderate earthquakes, GACOS-based correction can improve the coseismic deformation. In particular, the topography-correlated atmospheric errors can be reduced. For example, the 2016 Mw 5.9 Menyuan earthquake, the 2017 Mw 6.5 Jiuzhaigou earthquake, 2020 Mw 6.4 Yutian earthquake (Hong et al., 2018; Qu et al., 2021; Yu et al., 2020). However, in this case, for the 2020 Mw 5.7 Xegar earthquake, due to its location in Rikaze and the relatively dry climate, GACOS-based correction has little influence on

atmospheric errors. The GACOS-based corrections of the ascending and descending tracks were not obvious (Fig. S1). For the ascending track, the far-field deformation was slightly improved, but the effect was not good in some places. The magnitude of correction was less than 1 cm. For the descending track, most corrections were less than 5 mm. In order to clarify the impact of GACOS-based correction on the model, we either applied or did not apply GACOS-based correction to invert fault parameters, respectively. Both results are basically consistent, indicating that atmospheric correction has little effect on the model, and the convergence is better without correction of the model parameters (Figs. 3 and S2). Therefore, in this paper, we do not use GACOS-based correction.

4.3. The 2.5D Deformation Field and Dip Orientation

In the interior of the Tibetan Plateau, the Late Cenozoic faults are mainly strike-slip faults near the east–west direction and normal faults near the south–north direction, which are in sharp contrast to the main thrust shortening of the orogenic belt around the Tibetan Plateau (Molnar & Tapponnier, 1978; Molnar et al., 1993). The Xegar earthquake occurring in south Tibet is located near several basins, generating east–west tensile stress (Armijo et al., 1986, 1989).

To better understand the impact of the earthquake and facilitate the estimation of east–west and vertical displacement changes, we calculate the 2.5-dimensional (2.5D) deformation field. Because satellites are insensitive to the north–south direction, the LOS contribution of the north–south component is small (Wen et al., 2016), and its value (sine of azimuth angle) is almost negligible. Therefore, we can get the 2.5D deformation field (Guo et al., 2019; Xu et al., 2018; Yang et al., 2020), and the LOS displacements U associated with the orbits can be written as:

$$U \approx -\sin\theta\cos\emptyset U_e + \cos\theta U_u \qquad (2)$$

where U_e and U_u are quasi-eastward and quasi-upward displacements, respectively. In addition, θ is the radar incidence angle, and $\emptyset$ is the azimuth of the satellite heading vector.

According to the mechanism of normal faulting earthquakes, if the northeast-dipping fault plane is the optimal seismogenic plane, the east displacement values of the hanging wall will be much larger in the quasi-east–west displacement map. On the contrary, it is another case when the optimal seismogenic plane is southwest-dipping (Xu et al., 2018; Yang et al., 2020). The results of the 2.5D deformation field are shown in this study (Fig. 7). The eastern and western motions exhibit regional asymmetry, with maximum displacements of 7.1 and 5.1 cm, respectively, which
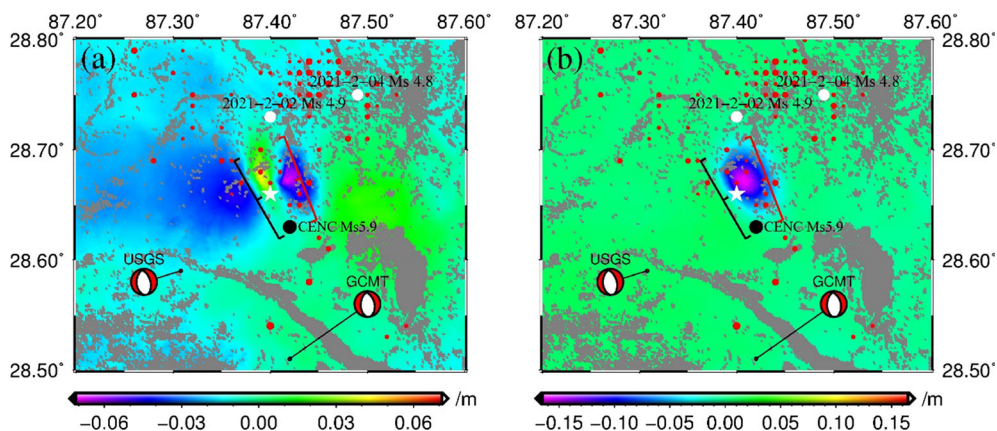

Figure 7
2.5 Dimensional deformation field maps. **a** and **b** are the coseismic quasi-east–west and quasi-vertical deformation maps, respectively. The black and red lines indicate the upper boundary of northeast-dipping and southwest-dipping models, respectively. White star and black circle indicate the epicenter location determined from InSAR and CENC, respectively. Two white circles indicate aftershocks of Mw 4.8 and Mw 4.9. The red circles represent aftershocks of less than Mw 4 (http://news.ceic.ac.cn/)

may explain the seismogenic fault being northeast-dipping. We also recognized that the aftershocks were more consistent with the northeast-dipping fault model (http://news.ceic.ac.cn/). In addition, we also calculated the uniform and distributed slip models of the southwest fault (Figs. S3–S5). In the distributed slip model, both the northeast-dipping and southwest-dipping fault models gave the RMS of the residuals for the ascending and descending Sentinel-1A datasets, resulting in average RMS residuals of 0.74 and 0.76 cm for the northeast- and southwest-dipping fault models, respectively (Figs. 4 and S6). Therefore, the fit of the northeast-dipping fault model is slightly better. For these reasons, we believe the seismogenic fault is northeast-dipping.

The coseismic quasi-vertical deformation with a maximum subsidence of 16.4 cm is mainly located in the hanging wall of the fault, indicating that this event has a predominantly normal mechanism. The distribution of inselbergs and the morphology of the edge of the basin indicate that the Tingri Basin is a rift basin that is still relatively subsiding (Li et al., 2004). The Xegar earthquake caused extension in the east–west direction of the Tingri Basin and the adjacent area, which is consistent with the expansion state presented by the surface strain rate field calculated by GPS data (Wang & Shen, 2020). In terms of the coseismic displacement of this earthquake, the characteristics of east–west movement and vertical movement may play a role in promoting the development of the basin.

4.4. The Impact of the 2015 Mw 7.9 Gorkha Earthquake

The 2020 Mw 5.7 Xegar earthquake struck the Tingri Basin in the Tibetan Plateau. In recent times, there has been considerable seismic activity in this area (Fig. 1). The 2015 Mw 7.9 Gorkha earthquake occurred in the surrounding area. The 2015 Ms 5.9 Tingri earthquake occurred $\sim$ 3 h after the Gorkha earthquake, and is located near the epicenter of the Xegar earthquake. Through calculation of the coseismic ΔCFS, many studies suggest that the Gorkha earthquake is responsible for triggering the 2015 Ms 5.9 Tingri earthquake (Li et al., 2017; Liu et al., 2017; Wan et al., 2015). Zha and Dai (2017)

calculated ΔCFS and seismicity rate changes on active faults on the Tibetan Plateau caused by the Gorkha earthquake, demonstrating the potentially high hazard presented by the South Tibet Detachment fault and its adjacent regions for triggering earthquakes. Therefore, does the Gorkha earthquake have an impact on the 2020 Xegar earthquake? To solve this problem, we estimate the impact of the Gorkha earthquake on the 2020 Xegar earthquake by calculating the coseismic and postseismic ΔCFS with different viscosities and depths.

We used the fault geometric parameters and slip distribution of the 2015 Gorkha earthquake obtained through the joint inversion of GPS and InSAR datasets (Fig. S7) (Tan et al., 2016). They are more accurate than the results obtained by seismic waves (Yagi et al., 2015; Hayes et al., 2017). We set the fault geometric parameters of the 2015 Gorkha earthquake as follows: strike = 285°, dip = 9°, length = 219 km, and width = 192 km; the fault plane was dispersed into 4672 sub-faults of 3×3 km. The preferred parameters of the 2020 Xegar earthquake were regarded as the receiver fault (strike 330.0°, dip 62.7°, and rake −109.2°). We chose empirical friction coefficient of 0.4 (King et al., 1994; Pollitz et al., 2006). The centroid location of the Xegar earthquake was set as the reference point (87.40° E, 28.66° N). Then, we utilized a linear Maxwell rheological model and used the software package PSGRN/PSCMP (Wang et al., 2006) to calculate the coseismic and postseismic relaxation ΔCFS of reference points with different depths (3.26 km and 5–20 km with an interval of 5 km) caused by the Gorkha earthquake. It is worth noting that an increase in ΔCFS by as little as 0.1 bar has been shown to be sufficient to encourage the occurrence of future earthquakes in regions where faults are critically stressed and close to failure (Stein, 1999).

First, the parameters used in the rheological model refer to Xiong et al. (2015) (Table S1). The viscosities of the middle-lower crust and the upper mantle were set as 1.0×10^{19} Pa·s and 1.0×10^{20} Pa·s. Within 20 years after the 2015 Mw 7.9 Gorkha earthquake, ΔCFS increased with time for depths of 3.26, 5, 10, and 15 km (Fig. 8). The value corresponding to a depth of 10 km is
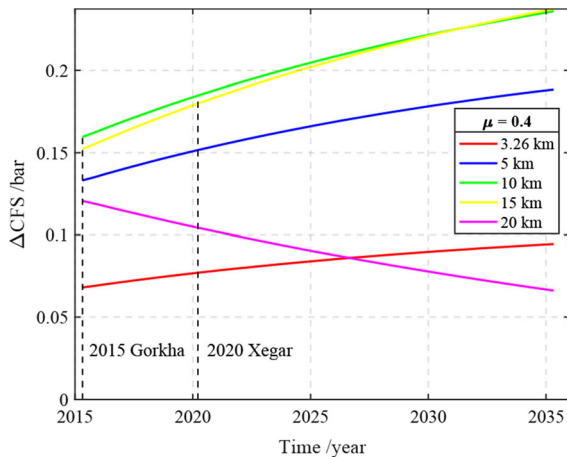
Figure 8
Curve of ΔCFS versus time at the centroid location of the 2020 Mw 5.7 Xegar earthquake caused by coseismic and postseismic viscoelastic relaxation of the 2015 Mw 7.9 Gorkha earthquake at different depths. The two dashed lines represent the 2015 Gorkha and the 2020 Xegar earthquakes, respectively

relatively large, with $\Delta CFS = \sim 0.185$ bar before the Xegar earthquake. At this time, the values of ΔCFS corresponding to 5 and 15 km are 0.152 and 0.180 bar, respectively. Their values of ΔCFS are higher than the earthquake triggering threshold of 0.1 bar, which indicates the possibility of triggering the Xegar earthquake. For a depth of 3.26 km (the depth corresponding to the maximum slip), the maximum ΔCFS is 0.077 bar before the Xegar earthquake. For depth of 20 km, ΔCFS continues to decrease as time increases, while the main rupture area of the Xegar earthquake is not within this range.

Then, in order to study the influence of rheology parameters, we calculated the ΔCFS with different rheology parameters. According to the study of Zha and Dai (2017), the coseismic stress changes below the Moho are too small, and the upper mantle viscosity is poorly constrained, so the viscosity is fixed with an empirical value of 1.0×10^{20} Pa•s. There are many studies on the viscosities of middle and lower crust in the Tibetan Plateau (Jiang et al., 2018; Zhang et al., 2009; Zhao et al., 2017). We simply separately set the viscosities of the middle and lower crust as 5.0×10^{18} Pa·s, 5.0×10^{19} Pa·s, 1.0×10^{20} Pa·s (Table S1). The results reveal that the magnitude of the ΔCFS changes with different viscosities (Fig. S8). The smaller the viscosity, the

faster the relaxation process. The detailed results were calculated with different viscosities and depths (Table S2). The higher the viscosity, the smaller the increase in ΔCFS at the centroid location of the 2020 Mw 5.7 Xegar earthquake. For depths of 5, 10 and 15 km, their values of ΔCFS are higher than 0.1 bar. In addition, we calculated the influence of different friction coefficients (Table S3).

Finally, we also considered the effect of afterslip. Hong et al. (2021) used InSAR and GPS data in a joint inversion for the evolution of afterslip; their results indicated that within 3 years of the Gorkha earthquake (from 15 May 2015 to 27 August 2018), afterslip released $\sim 1.20 \times 10^{20}$ Nm, or equivalent to an Mw 7.32 earthquake (Fig. S9). Therefore, we calculated the ΔCFS due to afterslip by 27 August 2018 at a depth of 3.26 km at the centroid location of the 2020 Xegar earthquake (Fig. S10). The ΔCFS due to afterslip is about 0.012 bar. Therefore, at a depth of 3.26 km, considering the influence of the 2015 Gorkha earthquake coseismic and postseismic relaxation and afterslip, the total ΔCFS at the centroid location of the Xegar earthquake is 0.089 bar. Although this is slightly less than the trigger stress threshold of 0.1 bar, according to Ziv and Rubin (2000), the lower limit of trigger stress is unknown; it has a certain promoting influence on the Xegar earthquake, which means that the coseismic and postseismic effects of the Gorkha earthquake may have triggered the Xegar earthquake.

In summary, according to our results, we suggest that the 2015 Gorkha earthquake played a key role in triggering the 2020 Mw 5.7 Xegar earthquake.

5. Conclusions

In this study, we used Sentinel-1A data to obtain the coseismic deformation field of the 2020 Mw 5.7 Xegar earthquake. The Bayesian method and SDM were used to invert the fault geometric parameters and coseismic slip distribution. ΔCFS was used to study the impact of the 2015 Gorkha earthquake on the 2020 Xegar earthquake. Thus, we have come to the following conclusions:

1. The LOS coseismic deformation field of the InSAR reveals that the main deformation area is dominated by subsidence. For ascending and descending tracks, the maximum displacements are 12.6 and 15.7 cm, respectively.

2. The inversion results indicate that the strike of the seismogenic fault is $\sim 330.0°$, the dip angle is $\sim 62.7°$, and the centroid location is (87.40° E, 28.66° N). Studies have revealed that the InSAR data in the near field can be used to determine the centroid location of moderate earthquakes.

3. According to the coseismic slip distribution, the main rupture zone covers an area of $\sim 5 \times 5 \text{ km}^2$ and only one slip asperity appears at a depth of 1.9–5.0 km. In addition, the mean rake angle is $\sim -104.6°$, and the maximum slip on the fault is 0.98 m at a depth of 3.26 km. The seismic moment released $\sim 3.23 \times 10^{17}$ Nm, or equivalent to Mw 5.6. The Xegar earthquake is dominated by normal faulting.

4. Based on the 2.5D displacement field, the coseismic eastern and western motions have maximum displacements of 7.1 and 5.1 cm, respectively. The coseismic quasi-vertical deformation has maximum subsidence of 16.4 cm. This may promote the development of the Tingri Basin to some extent. Our 2.5D displacement field, inversion results, and aftershock distribution all indicate that the seismogenic fault dips to the northeast.

5. We estimate the impact of the 2015 Mw 7.9 Gorkha earthquake on the 2020 Mw 5.7 Xegar earthquake by calculating the coseismic and postseismic ΔCFS with different viscosities and depths. The results suggest that the 2015 Gorkha earthquake played a key role in triggering the 2020 Mw 5.7 Xegar earthquake.

Acknowledgements

Funding

Data Availability

The datasets used during the current study are available from the corresponding author on reasonable request.

Declarations

REFERENCES

Armijo, R., Tapponnier, P., & Han, T. L. (1989). Late cenozoic right-lateral strike-slip faulting in southern Tibet. *Journal of Geophysical Research, 94*(B3), 2787–2838. https://doi.org/10.1029/JB094iB03p02787

Armijo, R., Tapponnier, P., Mercier, J., & Han, T. (1986). Quaternary extension in southern Tibet: Field observations and tectonic implications. *Journal of Geophysical Research,*

91(B14), 13803–13872. https://doi.org/10.1029/JB091iB14p13803

Chen, C. W., & Zebker, H. A. (2002). Phase unwrapping for large SAR interferograms: Statistical segmentation and generalized network models. *IEEE Transactions on Geoscience & Remote Sensing, 40*(8), 1709–1719. https://doi.org/10.1109/TGRS.2002.802453

Dan, Z., Zhu, D. F., Thubten, T., et al. (2016). Seismic tendency around the Tibet region after the 2015 M8.1 Nepal earthquake. *Earthquake Research in Sichuan, 2016*(2), 34–37. in Chinese.

Fadil, W., Lindsey, E. O., Wang, Y., Maung, P. M., Luo, H., Swe, T. L., Tun, P. P., & Wei, S. (2021). The January 11, 2018 Mw 6.0 Bago-Yoma myanmar earthquake: A shallow thrust event within the deforming bago-yoma range. *Journal of Geophysical Research: Solid Earth.* https://doi.org/10.1029/2020JB021313

Farr, T. G., Rosen, P. A., Caro, E., Crippen, R., Duren, R., Hensley, S., Kobrick, M., Paller, M., Rodriguez, E., & Roth, L. (2007). The shuttle radar topography mission. *Review of Geophysics, 45*(RG2004), 1–33. https://doi.org/10.1029/2005RG000183

Gao, H., Liao, M., & Feng, G. (2021). An improved quadtree sampling method for InSAR seismic deformation inversion. *Remote Sensing, 13*, 1678. https://doi.org/10.3390/rs13091678

Ghayournajarkar, N., & Fukushima, Y. (2022). Using InSAR for evaluating the accuracy of locations and focal mechanism solutions of local earthquake catalogues. *Geophysical Journal International, 230*(1), 607–622. https://doi.org/10.1093/gji/ggac072

Goldstein, R. M., & Werner, C. L. (1998). Radar interferogram filtering for geophysical applications. *Geophysical Research Letters, 25*(21), 4035–4038. https://doi.org/10.1029/1998GL900033

Guo, Z. L., Wen, Y. M., Xu, G. Y., et al. (2019). Fault slip model of the 2018 Mw 6.6 Hokkaido eastern Iburi, Japan, earthquake estimated from satellite Radar and GPS measurements. *Remote Sensing, 11*, 1667. https://doi.org/10.3390/rs11141667

Hayes, G. P. (2017). The finite, kinematic rupture properties of great-sized earthquakes since 1990. *Earth and Planetary Science Letters, 468*, 94–100. https://doi.org/10.1016/j.epsl.2017.04.003

Hong, S. Y., & Liu, M. (2021). Postseismic deformation and afterslip evolution of the 2015 Gorkha earthquake constrained by InSAR and GPS observations. *Journal of Geophysical Research: Solid Earth.* https://doi.org/10.1029/2020JB020230

Hong, S. Y., Zhou, X., Zhang, K., et al. (2018). Source model and stress disturbance of the 2017 Jiuzhaigou Mw 6.5 earthquake constrained by InSAR and GPS measurements. *Remote Sensing, 10*(1400), 1–19. https://doi.org/10.3390/rs10091400

Jiang, Z., Yuan, L., Huang, D., Yang, Z., & Hassan, A. (2018). Postseismic deformation associated with the 2015 Mw 7.8 Gorkha earthquake, Nepal: Investigating ongoing afterslip and constraining crustal rheology. *Journal of Asian Earth Sciences, 156*, 1–10. https://doi.org/10.1016/j.jseaes.2017.12.039

Jónsson, S., Zebker, H., Segall, P., & Amelung, F. (2002). Fault slip distribution of the 1999 Mw 7.2 Hector Mine earthquake, California, estimated from satellite radar and GPS measurements. *Bulletin of the Seismological Society of America, 92*(4), 1377–1389. https://doi.org/10.1785/0120000922

King, G., Stein, R., & Lin, J. (1994). Static stress changes and the triggering of earthquake. *Bulletin of the Seismological Society of America, 84*, 935–953. https://doi.org/10.1785/BSSA0840030935

Laske, G., Masters, G., Ma, Z., & Pasyanos, M. (2013). Update on CRUST1.0–A 1-degree global model of Earth's crust. *Geophysical Research Abstracts, 15*, EGU2013-2658.

Li, J. Z., Zhou, G. F., Feng, X. T., et al. (2004). Neo tectonism and environmental geohazards, Mt Zhumulangma area. *Journal of Geological Hazards & Environment Preservation, 15*(2), 6–10. in Chinese.

Li, L., Yao, D., Meng, X., Peng, Z., & Wang, B. (2017). Increasing seismicity in southern Tibet following the 2015 Mw 7.8 Gorkha, Nepal Earthquake. *Tectonophys, 714*, 62–70. https://doi.org/10.1016/j.tecto.2016.08.008

Li, Q., Tan, K., Wang, D. Z., et al. (2018). Joint inversion of GNSS and teleseismic data for the rupture process of the 2017 Mw6.5 Jiuzhaigou, China, earthquake. *Journal of Seismology, 22*(3), 805–814. https://doi.org/10.1007/s10950-018-9733-1

Liu, C., Dong, P. Y., & Shi, Y. L. (2017). Stress change from the 2015 Mw 7.8 Gorkha earthquake and increased hazard in the southern Tibetan Plateau. *Physics of the Earth & Planetary Interiors, 267*, 1–8. https://doi.org/10.1016/j.pepi.2017.04.002

Massonnet, D., Rossi, M., Carmona, C., Adragna, F., Peltzer, G., Feigl, K., & Rabaute, T. (1993). The displacement field of the Landers earthquake mapped by radar interferometry. *Nature, 364*(6433), 138–142. https://doi.org/10.1038/364138a0

Melgar, D., Geng, J., Crowell, B. W., Haase, J. S., Bock, Y., Hammond, W. C., & Allen, R. M. (2015). Seismogeodesy of the 2014 Mw6.1 Napa earthquake, California: Rapid response and modeling of fast rupture on a dipping strike-slip fault. *Journal of Geophysical Research: Solid Earth, 120*(7), 5013–5033. https://doi.org/10.1002/2015JB011921

Molnar, P., & Tapponnier, P. (1978). Active tectonics of Tibet. *Journal of Geophysical Research, 83*, 5361–5375. https://doi.org/10.1029/JB083iB11p05361

Molnar, P., England, P., & Martinod, J. (1993). Mantle dynamics, uplift of the Tibetan Plateau, and the Indian Monsoon. *Reviews of Geophysics, 31*(4), 357–396. https://doi.org/10.1029/93RG02030

Moral, P. D., Doucet, A., & Jasra, A. (2006). Sequential monte carlo samplers. *Journal of the Royal Statal Society, 68*(3), 411–436. https://doi.org/10.1111/j.1467-9868.2006.00553.x

Okada, Y. (1985). Surface deformation due to shear and tensile faults in a half-space. *Bulletin of the Seismological Society of America, 75*(4), 1135–1154. https://doi.org/10.1785/BSSA0750041135

Pollitz, F., Banerjee, P., Bürgmann, R., Hashimoto, M., & Choosakul, N. (2006). Stress change along the Sunda trench following the 26 December 2004 Sumatra-Andaman and 28 March 2005 Nias earthquakes. *Geophysical Research Letters, 33*, L06309. https://doi.org/10.1029/2005GL024558

Qu, W., Liu, B., Zhang, Q., et al. (2021). Sentinel-1 InSAR observations of co-and post-seismic deformation mechanisms of the 2016 Mw 5.9 Menyuan Earthquake. *Northwestern China. Advances in Space Research, 68*(3), 1301–1317. https://doi.org/10.1016/j.asr.2021.03.016

Rosen, P. A., Gurrola, E., Sacco, G. F., & Zebker, H. (2012). The InSAR scientific computing environment. *EUSAR 2012. 9th European Conference on Synthetic Aperture Radar*, 730–733

Stein, R. S. (1999). The role of stress transfer in earthquake occurrence. *Nature, 402*(6762), 605–609. https://doi.org/10.1038/45144

Tan, K., Zhao, B., Zhang, C. H., et al. (2016). Rupture models of the Nepal Mw7.9 earthquake and Mw7.3 aftershock constrained by GPS and InSAR coseismic deformations. *Chinese Journal Geophysics, 59*(6), 2080–2093. in Chinese.

Vasyura-Bathke, H., Dettmer, J., Steinberg, A., Heimann, S., Isken, M. P., Zielke, O., Mai, P. M., Sudhaus, H., & Jónsson, S. (2020). The Bayesian earthquake analysis tool. *Seismological Research Letters, 91*, 1003–1018. https://doi.org/10.1785/0220190075

Wang, R., Lorenzo-Martín, F., & Roth, F. (2006). PSGRN/PSCMP—a new code for calculating co-and post-seismic deformation, geoid and gravity changes based on the viscoelastic-gravitational dislocation theory. *Computers & Geosciences, 32*(4), 527–541. https://doi.org/10.1016/j.cageo.2005.08.006

Wan, Y. G., Sheng, S. Z., Li, X., et al. (2015). Stress influence of the 2015 Nepal earthquake sequence on Chinese mainland. *Chinese Journal Geophysics, 58*(11), 4277–4286. in Chinese.

Wang, M., & Shen, Z. K. (2020). Present-day crustal deformation of continental China derived from GPS and its tectonic implications. *Journal of Geophysical Research: Solid Earth*. https://doi.org/10.1029/2019JB018774

Wang, R. J., Martin, F. L., & Roth, F. (2003). Computation of deformation induced by earthquakes in a multi-layered elastic crust-FORTRAN programs EDGRN/EDCMP. *Computers & Geosciences, 29*(2), 195–207. https://doi.org/10.1016/S0098-3004(02)00111-5

Wang, Q., Qiao, X. J., Lan, Q. G., et al. (2011). Rupture of deep faults in the 2008 Wenchuan earthquake and uplift of the Longmen Shan. *Nature Geoscience, 4*(9), 634–640. https://doi.org/10.1038/ngeo1210

Wang, S., Xu, C., Li, Z., Wen, Y., & Song, C. (2020). The 2018 Mw 7.5 Papua New Guinea earthquake: A possible complex multiple faults failure event with deep-seated reverse faulting. *Earth & Space Science*. https://doi.org/10.1029/2019EA000966

Wang, R., Diao, F., & Hoechner, A. (2013). SDM–a geodetic inversion code incorporating with layered crust structure and curved fault geometry. *EGU General Assembly*, 15, EGU2013–2411-1

Wen, Y. M., Xu, C. J., Liu, Y., et al. (2016). Deformation and source parameters of the 2015 Mw 6.5 earthquake in Pishan, Western China, from Sentinel-1A and ALOS-2 data. *Remote Sensing, 8*(2), 134. https://doi.org/10.3390/rs8020134

Wessel, P., Smith, W. H., Scharroo, R., Luis, J., & Wobbe, F. (2013). Generic mapping tools: Improved version released. *Eos, Transactions of the American Geophysical Union, 94*(45), 409–410. https://doi.org/10.1002/2013EO450001

Weston, J., Ferreira, A. M. G., & Funning, G. J. (2011). Global compilation of interferometric synthetic aperture radar earthquake source models: 1 comparisons with seismic catalogs. *Journal of Geophysical Research: Solid Earth*. https://doi.org/10.1029/2010JB008131

Weston, J., Ferreira, A. M. G., & Funning, G. J. (2012). Systematic comparisons of earthquake source models determined using InSAR and seismic data. *Tectonophysics, 532*, 61–81. https://doi.org/10.1016/j.tecto.2012.02.001

Xiong, W., Tan, K., Liu, G., Qiao, X., & Nie, Z. (2015). Coseismic and postseismic Coulomb stress changes on surrounding major faults caused by the 2015 Nepal Mw 7.9 earthquake. *Chinese Journal Geophysics, 58*(11), 4305–4316. in Chinese.

Xu, G. Y., Xu, C. J., & Wen, Y. M. (2018). Sentinel-1 observation of the 2017 Sangsefid earthquake, northeastern Iran: Rupture of a blind reserve-slip fault near the Eastern Kopeh Dagh. *Tectonophysics, 731*, 131–138. https://doi.org/10.1016/j.tecto.2018.03.009

Yagi, Y., & Okuwaki, R. (2015). Integrated seismic source model of the 2015 Gorkha, Nepal, earthquake. *Geophysical Research Letters*. https://doi.org/10.1002/2015GL064995

Yang, J., Xu, C., Wang, S., & Wang, X. (2020). Sentinel-1 observation of 2019 Mw 5.7 Acipayam earthquake: A blind normal-faulting event in the Acipayam basin, southwestern Turkey. *Journal of Geodynamics, 135*, 101707. https://doi.org/10.1016/j.jog.2020.101707

Yong, Y. Y. (2012). The NS-trending structures in the southwestern part of the Qinghai-Xizang Plateau: New insights. *Sedimentary Geology & Tethyan Geology, 32*(3), 21–30. in Chinese.

Yu, C., Penna, N. T., & Li, Z. (2017). Generation of real-time mode high-resolution water vapor fields from GPS observations. *Journal of Geophysical Research: Atmospheres, 122*, 2008–2025. https://doi.org/10.1002/2016JD025753

Yu, C., Li, Z., & Penna, N. T. (2018). Interferometric synthetic aperture radar atmospheric correction using a GPS-based iterative tropospheric decomposition model. *Remote Sensing of Environment, 204*, 109–121. https://doi.org/10.1016/j.rse.2017.10.038

Yu, J., Zhao, B., Xu, W., & Tan, K. (2020). Oblique fault movement during the 2016 Mw 5.9 Zaduo earthquake: Insights into regional tectonics of the Qiangtang block, Tibetan Plateau. *Journal of Seismology, 24*, 693–708. https://doi.org/10.1007/s10950-020-09930-7

Zha, X. J., & Dai, Z. Y. (2017). Using geodetic data to calculate stress changes on faults in the Tibetan Plateau caused by the 2015 Mw7.8 Nepal earthquake. *Journal of Asian Earth Sciences, 133*, 38–45. https://doi.org/10.1016/j.jseaes.2016.11.009

Zhang, J. J., Guo, L., & Ding, L. (2002). Structural characteristics of middle and southern Xainza-Dingye normal fault system and its relationship to Southern Tibetan detachment system. *Chinese Science Bulletin, 47*(10), 738–743. in Chinese.

Zhang, C., Cao, J., & Shi, Y. (2009). Studying the viscosity of lower crust of Qinghai-Tibet Plateau according to post-seismic deformation. *Science in China Series D: Earth Sciences, 52*, 411–419. in Chinese.

Zhao, B., Bürgmann, R., Wang, D., Tan, K., Du, R., & Zhang, R. (2017). Dominant controls of downdip afterslip and viscous relaxation on the postseismic displacements following the Mw7.9 Gorkha, Nepal, earthquake. *Journal of Geophysical Research, 122*, 8376–8401. https://doi.org/10.1002/2017JB014366

Zhao, D., Qu, C., Shan, X., Gong, W., Zhang, G., & Song, X. (2019). New insights into the 2010 Yushu Mw6. 9 mainshock and Mw5.8 aftershock, China, from InSAR observations and inversion. *Journal of Geodynamics, 125*, 22–31. https://doi.org/10.1016/j.jog.2019.01.008

Zhu, C., Wang, C., Zhang, B., Qin, X., & Shan, X. (2021). Differential interferometric synthetic aperture radar data for more accurate earthquake catalogs. *Remote Sensing of Environment, 266*, 112690. https://doi.org/10.1016/j.rse.2021.112690

Ziv, A., & Rubin, A. M. (2000). Static stress transfer and earthquake triggering: No lower threshold in sight? *Journal of Geophysical Research Solid Earth, 105*, 13631–13642. https://doi.org/10.1029/2000JB900081